Two-dimensional crystal phases of graphene monoxide

Danylo Radevych,* Marija Gajdardziska-Josifovska,† and Michael Weinert‡
University of Wisconsin-Milwaukee, Department of Physics, 3135 N Maryland Ave, Milwaukee, Wisconsin 53211, USA

(Received 21 December 2022; accepted 30 January 2023; published 14 February 2023)

The possible existence and properties of different polytypes of graphene monoxide (GmO)—two-dimensional crystalline monolayers composed of equal numbers of C and O atoms—are investigated using density functional calculations. Structural parameters, electronic, and mechanical properties of the different phases, including the previously reported α and β phases, are determined and compared. It is suggested that multiple phases of GmO can coexist in the same composite, but developing a synthesis process for single-phase GmO may be experimentally challenging. The phases exhibit band structures ranging from insulating to metallic. From an analysis of the calculated elastic moduli, it is concluded that all the GmO structures are softer than graphene and are likely to change their lattice parameters if present in a composite with graphene.

DOI: 10.1103/PhysRevB.107.054104

I. INTRODUCTION

The name graphene monoxide (GmO) was introduced in 2011 to denote a solid crystalline form of a two-dimensional monolayer with equal number of C and O atoms in a centered rectangular structure (distorted graphene). The calculated semiconducting properties suggested opportunities for new applications in electronics, sensors, and energy storage, particularly considering its compatibility with graphene and graphite [1].

Although the names "graphene monoxide" and "graphene oxide" (GO) are similar, they represent different materials with distinct properties. In GO [2–5], various oxygen functional groups (e.g., epoxide C–O–C, carbonyl C=O, hydroxyl C–OH, and carboxyl OH–C=O) are randomly distributed on the graphene lattice. The O to C ratios in GO (which depend critically on the preparation technique) are significantly less than one; reduced GO (rGO), with even lower O : C ratios, is a commonly used precursor in the production of graphene. In contrast, in GmO the O atoms are arranged periodically and O : C = 1 by definition.

By stoichiometry, GmO is the same as carbon monoxide (CO). CO is a gas at ambient conditions, but can solidify in a range of three-dimensional crystal phases at low temperatures and/or high pressures. Unlike CO, however, two-dimensional GmO is a solid at a wide range of temperatures and pressures, including ambient. Inspired by a recent experimental discovery of a second GmO phase [6], the main question addressed in the present systematic computational study is whether multiple stable two-dimensional (2D) crystal phases of GmO exist. The goal is to predict the range of structural, mechanical, and electronic properties that can be expected in the GmO family of phases to facilitate the future creation and applications of such materials.

The first two known members of the GmO family—α- and β-GmO—are built out of 1,3-dioxetane units [Fig. 1(a)] into structures shown in Figs. 2(a) and 2(b). These phases were found in experiments at ambient conditions [1,6] and described via density functional theory (DFT) modeling [1,6–11]. The α-GmO phase has one 1,3-dioxetane per 2D primitive cell and is distinguished from graphene by its nonzero band gap that can be tuned by applied strain [8] or defects [12]. Computational investigation of the interaction of Li with α-GmO showed that electron transfer shifted the Fermi level and turned α-GmO into a conductor [13] and also reported a larger theoretical Li capacity for α-GmO than for graphene or graphite, suggesting that α-GmO is a promising candidate as a Li-ion battery anode material. Modeling of α-GmO bilayers suggested further applications in switching media for nanoelectronics [14]. The β-GmO phase, consisting of three 1,3-dioxetanes per primitive 2D unit cell, was discovered to coexist with α-GmO and graphene in the same composite under certain synthesis conditions and predicted to be semiconducting [6]. The present work reports the first complete study of the elastic properties of α- and β-GmO.

To probe the possibility of occurrence of more than two stable phases of GmO, we start by focusing on the similarities between the α- and β-GmO structures and use *ab initio* modeling to check if other monolayers made of the same 1,3-dioxetane building units that form the α and β phases could exist. Additionally, potential monolayers made of other building blocks [C–O–C epoxides, C–O–C-ether-like links, double-bonded C=C pairs, and C=O carbonyls in Figs. 1(b) to 1(e)] were constructed to test whether GmO needed to be built exclusively of 1,3-dioxetanes. One model that had 1,3-dioxetanes, epoxides, and C–O–C-ether-like links at the same time was taken from the *ab initio* searching results of Xiang *et al.* [10]. Of the investigated monolayer structures, only those with negative formation energies are reported here.

*radevych@uwm.edu
†mgj@uwm.edu
‡weinert@uwm.edu

 ©2023 American Physical Society

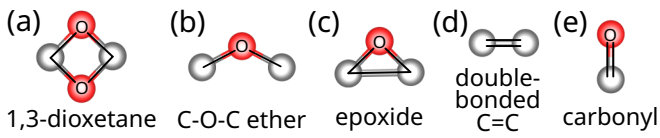

FIG. 1. Building units of the GmO phases: (a) 1,3-dioxetane, (b) C–O–C ether, (c) C–O–C epoxide, (d) double-bonded C=C, and (e) carbonyl. (C: gray; O: red.)

In the history of three-dimensional (3D) CO solids, pressure versus temperature (P-T) phase diagram and polymerization were studied in many experimental papers [15–26]. The phase diagram has four molecular solid phases of 3D CO—$\alpha(P2_13)$, $\beta(P6_3/mmc)$, $\delta(Pm3n)$, and $\varepsilon(R3c)$, as well as a variety of polymeric CO phases. Although CO and N_2 solids were initially believed to be similar due to similarities between their experimentally discovered α and β phases, a CO structure equivalent to the $\gamma(P4_2/mnm)$ phase of N_2 was never found [15]. In contrast to the Greek-letter naming convention, the most recent *ab initio* papers that employ searching methods to predict novel structures of solid CO (which have not been confirmed experimentally) refer to the structures by the corresponding space groups [27,28]. Following the naming convention from the CO papers, α- and β-GmO were assigned Greek letters based on the order of their experimental discovery and the other phases discussed in the present study are distinguished by their space groups.

In experiments, α-GmO is found with modified lattice parameters compared to the relaxed DFT structure, likely because α-GmO is in a composite with graphene [1,6]. Electronic band-structure calculations suggested that such a deformed state would be metallic [6,8], unlike the semiconducting relaxed state. Because GmO is most often found in composites, the elastic constants were computed to determine how soft the GmO phases are and whether structures are stable under applied deformations.

II. METHODS

A. DFT simulations: Structure and electronic properties

DFT simulations were performed with Quantum ESPRESSO 7.0 [29–31]. Structures under consideration were visualized via VESTA 3.5.0 [32]. For C and O atoms, projector augmented-wave (PAW) scalar-relativistic pseudopotentials with the Perdew-Burke-Ernzerhof (PBE) generalized gradient approximation (GGA) for exchange-correlation were taken from PSLIBRARY 1.0.0 [33]. A plane-wave kinetic energy cutoff for wave functions and kinetic energy cutoff for charge density and potential were 50 Ry (680 eV) and 326 Ry (4435 eV), respectively. The $18 \times 18 \times 1$ Monkhorst-Pack k-point meshes were utilized for rhombic primitive cells of graphene and α-GmO, while k-meshes for unit cells and corresponding supercells (including centered rectangular) of other structures were rescaled accordingly. The interlayer spacing for monolayer computations was fixed at 25 Å.

Possible changes to the structures due to the inclusion of weak van der Waals (vdW) forces were investigated using the DFT-D3 (BJ) correction [34,35]. While GGA functionals are well suited for description of the in-plane distances in graphene, they struggle with the interlayer spacing in graphite [36]. Our choice of PBE + DFT-D3 (BJ) for the vdW correction in some GmO phases was motivated by the comparison [37] of different vdW corrections that concluded that the DFT-D3 (BJ) correction provided the results closest to experiment for the stacking of hexagonal boron nitride and graphite. Because in-plane distances were found not to be sensitive to the DFT-D3 (BJ) correction, the vdW results were reported only where they were relevant.

All the investigated GmO models had different symmetries and could be uniquely identified by their space groups. Space groups of the models were verified with the FINDSYM 7.1.4 software [38,39]. Lattice parameters and atomic (Wyckoff) positions were given consistent with the "International Tables for Crystallography" [40] and crystallographic data (e.g., [41]).

For the electronic structure calculations, a band-unfolding technique was applied [42–45]. The electronic bands of all GmO phases were unfolded onto an equivalent first Brillouin zone corresponding to the rhombic primitive cell of the graphene or α-GmO monolayers. Then bands were calculated along the same $M \to \Gamma \to K$ path in reciprocal space.

B. Elastic moduli from DFT

Definitions of elastic constants differ in the literature. To avoid confusion and to explain the notation used here, a brief summary of the standard theory of elasticity, adopted to the 2D case, is provided.

In the general 3D case, the stress dependence on the strain is expressed through

$$\boldsymbol{\sigma} = \hat{C}\boldsymbol{\varepsilon} \tag{1}$$

$$\begin{bmatrix} \sigma_{xx} \\ \sigma_{yy} \\ \sigma_{zz} \\ \sigma_{yz} \\ \sigma_{zx} \\ \sigma_{xy} \end{bmatrix} = \begin{bmatrix} C_{11} & C_{12} & C_{13} & C_{14} & C_{16} \\ C_{21} & C_{22} & C_{23} & C_{24} & C_{26} \\ C_{31} & C_{32} & C_{33} & C_{34} & C_{36} \\ C_{41} & C_{42} & C_{43} & C_{44} & C_{46} \\ C_{51} & C_{52} & C_{53} & C_{54} & C_{56} \\ C_{61} & C_{62} & C_{63} & C_{64} & C_{66} \end{bmatrix} \begin{bmatrix} \varepsilon_{xx} \\ \varepsilon_{yy} \\ \varepsilon_{zz} \\ \varepsilon_{yz} \\ \varepsilon_{zx} \\ \varepsilon_{xy} \end{bmatrix}, \tag{2}$$

where $\boldsymbol{\sigma}$ is a six-component stress column vector, $\boldsymbol{\varepsilon}$ is a six-component column vector of strains, $\hat{C}$ is a 6×6 symmetric elastic stiffness matrix ($C_{ij} = C_{ji}$, $xx = 1$, $yy = 2$, $zz = 3$, $yz = zy = 4$, $zx = xz = 5$, $xy = yx = 6$), and $\sigma_{\alpha\beta}$ represents a force applied in the α direction to a unit area of a plane whose normal lies in the β direction [46].

In the Voigt notation, the strains ε_i are expressed through the deformation coefficients δ_i of the transformation matrix $\hat{D}$:

$$\varepsilon_i = \xi_i \delta_i = \begin{cases} \delta_i, & \text{if } i = 1, 2, 3, \\ 2\delta_i, & \text{if } i = 4, 5, 6, \end{cases} \tag{3}$$

$$\hat{D} = \begin{bmatrix} 1+\delta_1 & \delta_6 & \delta_5 \\ \delta_6 & 1+\delta_2 & \delta_4 \\ \delta_5 & \delta_4 & 1+\delta_3 \end{bmatrix}, \tag{4}$$

where $\xi_i = 1$ for $i = 1, 2, 3$, or 2 for $i = 4, 5, 6$. $\hat{D}$ acts on the matrix of the original lattice vectors $\hat{R}$ and distorts it to $\hat{R}'$, i.e., $\hat{R}' = \hat{D}\hat{R}$ [47,48]. Even if the original lattice vectors in $\hat{R}$ are orthogonal, the deformed lattice vectors $\hat{R}'$ generally are not.

The total energy in the Voigt notation is

$$E(V,\boldsymbol{\delta}) = E(V_0,\mathbf{0}) + V_0\left(\sum_{i=1}^{6}\tau_i\xi_i\delta_i + \frac{1}{2}\sum_{i=1}^{6}\sum_{j=1}^{6}C_{ij}\xi_i\delta_i\xi_j\delta_j\right), \quad (5)$$

where τ_i are components of the stress tensor.

For our purposes, we adopt rectangular or centered rectangular unit cells of the candidate 2D structures. For a rectangular or centered rectangular 2D cell ($\boldsymbol{a} \perp \boldsymbol{b}$), the elastic stiffness matrix $\hat{C}$ reduces to a 3×3 matrix and the transformation matrix $\hat{D}$ becomes 2×2 (all z-related components with indices 3, 4, and 5 drop out):

$$\begin{bmatrix}\sigma_1\\ \sigma_2\\ \sigma_6\end{bmatrix} = \begin{bmatrix}C_{11} & C_{12} & 0\\ C_{12} & C_{22} & 0\\ 0 & 0 & C_{66}\end{bmatrix}\begin{bmatrix}\delta_1\\ \delta_2\\ 2\delta_6\end{bmatrix}, \quad (6)$$

with the transformation of the perpendicular in-plane lattice vectors $\boldsymbol{a}$ and $\boldsymbol{b}$ to $\boldsymbol{a}'$ and $\boldsymbol{b}'$ given by

$$\begin{bmatrix}a'_x & a'_y\\ b'_x & b'_y\end{bmatrix} = \begin{bmatrix}1+\delta_1 & \delta_6\\ \delta_6 & 1+\delta_2\end{bmatrix}\begin{bmatrix}a & 0\\ 0 & b\end{bmatrix}. \quad (7)$$

For this reason, the four elastic stiffness constants—C_{11}, C_{22}, C_{12}, and C_{66}—are sufficient to describe the elastic properties of these monolayers.

The elastic stiffness constants are obtained from the second derivatives of the total energies E with respect to the four distortions

$$\hat{D}_{11} = \begin{bmatrix}1+\delta & 0\\ 0 & 1\end{bmatrix} \rightarrow C_{11} = \left.\frac{d^2E}{d\delta^2}\right|_{\delta=0} \quad (8)$$

$$\hat{D}_{22} = \begin{bmatrix}1 & 0\\ 0 & 1+\delta\end{bmatrix} \rightarrow C_{22} = \left.\frac{d^2E}{d\delta^2}\right|_{\delta=0} \quad (9)$$

$$\hat{D}_{12} = \begin{bmatrix}1+\delta & 0\\ 0 & 1-\delta\end{bmatrix} \rightarrow 2C_{12} = C_{11} + C_{22} - \left.\frac{d^2E}{d\delta^2}\right|_{\delta=0} \quad (10)$$

$$\hat{D}_{66} = \begin{bmatrix}1 & \delta\\ \delta & 1\end{bmatrix} \rightarrow C_{66} \equiv G_{2D} = \frac{1}{4}\left.\frac{d^2E}{d\delta^2}\right|_{\delta=0}. \quad (11)$$

The elastic constants C_{11} and C_{22} correspond to the cell being deformed along the $\boldsymbol{a}$ and $\boldsymbol{b}$ lattice vectors, respectively, while the perpendicular lattice vectors ($\boldsymbol{b}$ and $\boldsymbol{a}$) stay fixed.

C_{12} corresponds to a distortion that increases a and decreases b, and $C_{66} \equiv G_{2D}$ is a 2D shear modulus [49]. For hexagonal symmetry, as in the case of graphene, $C_{11} = C_{22}$ and $C_{66} \equiv G_{2D} = 1/2(C_{11} - C_{12})$, so there are only two unique elastic stiffness constants [50].

Related to C_{11} and C_{22}, the 2D Young's moduli Y_1 and Y_2 correspond to transformations in which the lattice vectors $\boldsymbol{b}$ and $\boldsymbol{a}$ are allowed to relax as the vectors $\boldsymbol{a}$ and $\boldsymbol{b}$ (respectively) are being pulled, i.e., Y_1 and Y_2 include the effect of the Poisson ratio. The 2D Young's moduli can be computed from the elastic constants via [51] (see [52] for the derivation)

$$Y_1 = \frac{C_{11}C_{22} - C_{12}^2}{C_{22}}, \qquad Y_2 = \frac{C_{11}C_{22} - C_{12}^2}{C_{11}}. \quad (12)$$

In analogy to the 3D bulk modulus, we define the 2D bulk modulus B_{2D} to be proportional to the second derivative of the energy E with respect to the area of the cell S, or equivalently, to the deformation

$$\hat{D}_{B_{2D}} = \begin{bmatrix}1+\delta & 0\\ 0 & 1+\delta\end{bmatrix}, \quad (13)$$

$$B_{2D} = S_0\left.\frac{\partial^2E}{\partial S^2}\right|_{S=S_0} = \frac{1}{4S_0}\left.\frac{\partial^2E}{\partial\delta^2}\right|_{\delta=0} = \frac{C_{11}+C_{22}+2C_{12}}{4}. \quad (14)$$

This definition is analogous to the layer modulus introduced in [51] and gives results for graphene that are in agreement with the 2D bulk modulus reported in [53]. Note that B_{2D} defined this way is two times smaller than the biaxial elastic constant [54,55] generated by the same transformation and can be expressed through the constants C_{11}, C_{22}, and C_{12} without the need to explicitly use the transformation $\hat{D}_{B_{2D}}$.

In the actual calculations, the total energies $E(\delta)$ were calculated for a set of small deformations $|\delta| < 0.01$ for each of the deformations described in Eqs. (8) to (11). Finally, the elastic constants were determined from the second derivatives of $E(\delta)$ as described above.

III. RESULTS

A. Modeled phases

The GmO phases discussed here were built from one or more of five units—1,3-dioxetane, C–O–C ether, epoxide, double-bonded C=C, and carbonyl (see Fig. 1). In addition, the structures had to be 2D in nature and have equal numbers of C and O atoms.

The first group of GmO phases are monolayers that have C atoms with four bonds (sp^3) [Figs. 2(a) to 2(d)]: α-, β-, *Pmam*-, and *Cmm*2-GmO.

α-GmO [Fig. 2(a)] was the first experimentally observed form of GmO, determined by selected area electron diffraction (SAED) measurements and DFT modeling [1] and also obtained in an *ab initio* structure search [10]. The α-GmO structure is built from 1,3-dioxetane units [Figs. 1(a) and 3(a)], with C atoms in the xy plane and O atoms above and below such that the planes of 1,3-dioxetanes are perpendicular to the center plane of the monolayer. The calculated relaxed structure of α-GmO has space group *Cmmm*, with a lattice constant of 3.13 Å and opening angle of 130°. Experimentally, α-GmO was found in a composite with graphene, with an average lattice constant of 2.95 Å and opening angle of ∼120° [6]. Based on the opening angle, experimental α-GmO is referred to as α-GmO^{120}. Although the lattice parameters

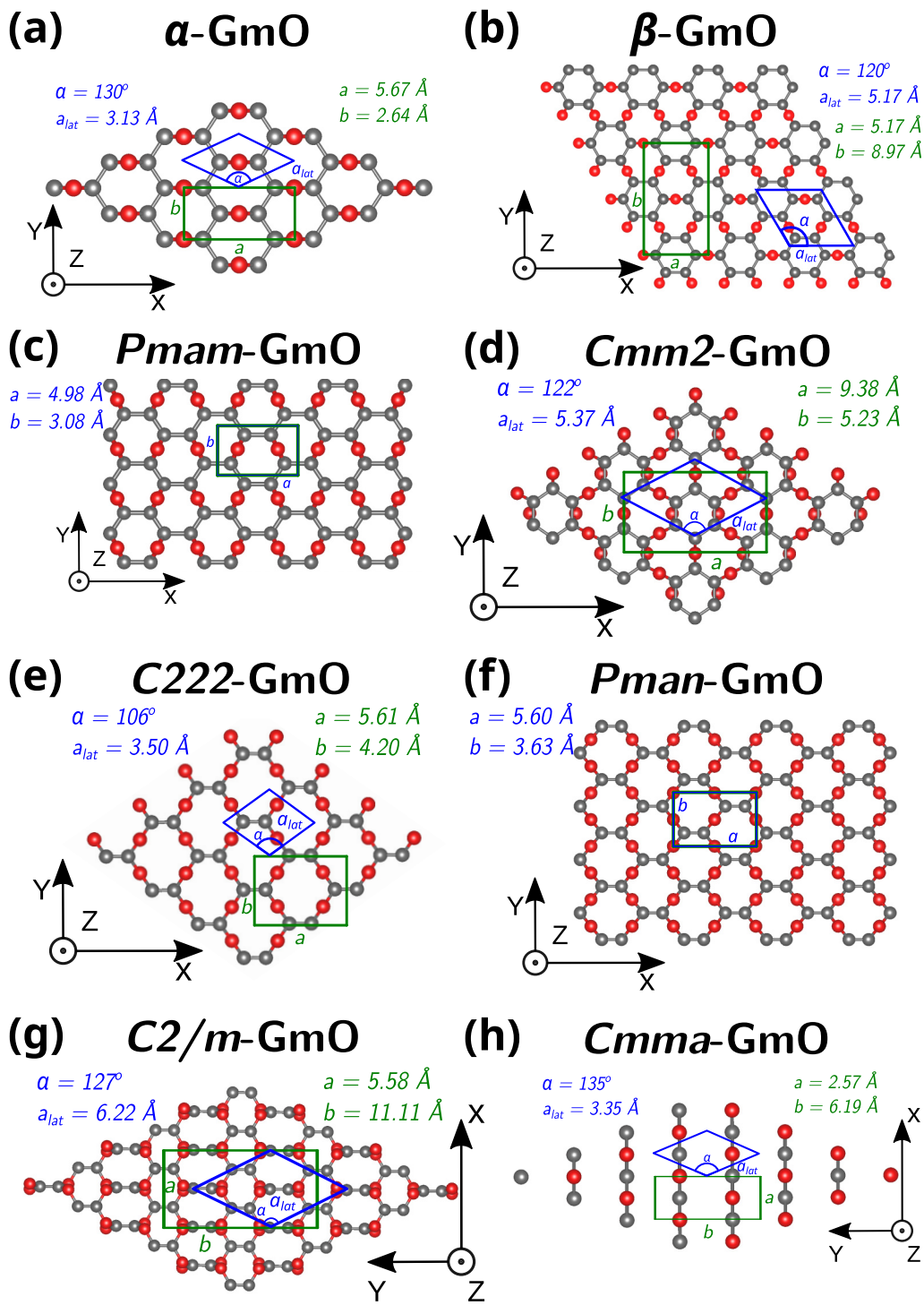

FIG. 2. Phases of GmO. Structures containing C atoms with four bonds: (a) α-, (b) β-, (c) *Pmam*-, and (d) *Cmm*2-GmO. Structures containing C atoms with three bonds: (e) *C*222-, (f) *Pman*-, (g) *C*2/*m*-, and (h) *Cmma*-GmO. Top view. Axes orientation in (g) and (h) is different from other figures. (Primitive cell: blue; rectangular or centered rectangular cell: green; C: gray; O: red. See [52] for other views.)

appear to be quite different, the areas of the primitive cells of *ab initio* α-GmO and experimental α-GmO^{120} are essentially the same, indicating that α-GmO in the composite adjusted its lattice parameters, while conserving the area, to coexist with graphene. From DFT, the formation energy of relaxed α-GmO is -0.58 eV/atom [10], while the corresponding value for α-GmO^{120} is 0.26 eV/atom less negative (-0.32 eV) [6], in line with our present results.

With a formation energy of -0.51 eV/atom, β-GmO [Fig. 2(b)] is also built of 1,3-dioxetane units that are perpendicular to the center plane of C atoms. The difference between the two structures is that the planes of 1,3-dioxetanes

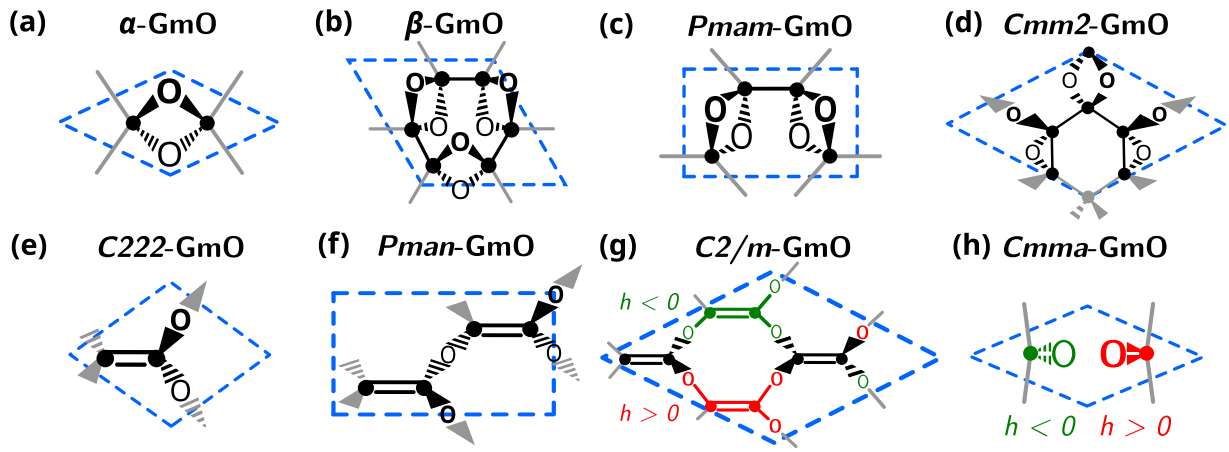

FIG. 3. Skeletal structures of the primitive cells of different phases of GmO: (a) α-, (b) β-, (c) *Pmam*-, (d) *Cmm*2-, (e) *C*222-, (f) *Pman*-, (g) *C*2/*m*-, and (h) *Cmma*-GmO. O atoms are given explicitly, C atoms are marked with solid circles. Solid triangular bonds go above the center plane, dashed triangular bonds go below the center plane. Skeletal representation of primitive atoms and bonds: black; periodic continuation: gray. In *C*2/*m*- and *Cmma*-GmO, red and green colors show groups of atoms above and below the center plane, respectively. Primitive cell borders (dashed blue) and bonds are not drawn to scale.

in β-GmO are aligned not just in one direction (as in α-GmO), but in three directions differing by a 120° rotation. The rhombic (hexagonal) primitive cell contains six C and six O atoms, with a lattice constant of 5.17 Å; when considered as a $\sqrt{3} \times \sqrt{3}$ supercell of α-GmO, its corresponding primitive lattice constant is 2.98 Å, close to that of α-GmO[120]. The space group of β-GmO is $P6/mmm$, the same as of graphene. Notably, β-GmO is the most symmetric form among all phases of GmO considered in this work.

As was suggested in [6], the mechanism for α- and β-GmO formation can be thought of as based on the substitution of double bonds (C=C) in graphene by O pairs and the formation of out-of-plane 1,3-dioxetane units. Double bonds in an infinite monolayer of graphene can be aligned in one of the three equivalent armchair directions [Fig. 4(a)], in two [Fig. 4(b)], or in all three at the same time [Fig. 4(c)]. Based on this assumption, α- and β-GmO phases correspond to Figs. 4(a) and 4(c), respectively. A phase corresponding to Fig. 4(b), with space-group symmetry *Pmam*, has not been discussed previously.

In *Pmam*-GmO [Fig. 2(c)], two 1,3-dioxetane units, rotated by ∼50° around the z axis with respect to each other, form a rectangular primitive cell [Fig. 3(c)], with four C and four O atoms, and lattice constants $a = 4.98$ Å and $b = 3.08$ Å, in contrast to the one and three units forming the rhombic primitive cells of α- and β-GmO, respectively. The planes of 1,3-dioxetanes are also perpendicular to the center plane of the monolayer formed by C atoms. The formation energy of −0.52 eV is only 0.01 eV more negative than for β-GmO and 0.20 eV more negative than in experimental α-GmO[120], suggesting that the creation of β- and *Pmam*-GmO is energetically equivalent and more energetically favorable than the creation of α-GmO[120]. The similarities in the structures of α-, β-, and *Pmam*-GmO, as well as energy analysis, hint that *Pmam*-GmO likely could be found experimentally if proper synthesis conditions were found.

Xiang *et al.* [10] reported, in addition to α-GmO (D_{2h} C_1O), another possible GmO structure with a more negative formation energy of −0.61 eV/atom with C_{2v} point-group symmetry. In our simulations, we reproduced this structure and the previously reported formation energy. For consistency in our naming, this structure is labeled as *Cmm*2-GmO [Fig. 2(d)]. The rhombic primitive cell of *Cmm*2-GmO [Fig. 3(d)] has a lattice constant of 5.37 Å and opening angle of 122°. The structure is built up from one 1,3-dioxetane, two epoxides [Fig. 1(c)], and two linking O atoms. Each linking O atom is attached to two epoxides such that, together with corresponding two C atoms, they resemble a C–O–C ether, where there is no physical bond between the two C atoms [Fig. 3(b)]. A plane of the 1,3-dioxetane and C–C bonds in two epoxides are aligned in the same direction. The plane of the 1,3-dioxetane is perpendicular to the center plane of the monolayer formed by C atoms, while planes of the epoxides are tilted by 12° with respect to the plane of 1,3-dioxetane. The O atoms of the epoxides are placed below the center plane. Each linking O atom is located above the center plane. The planes of C–O–C-ether-like parts are perpendicular to the center plane. With six C and six O atoms, the total number of

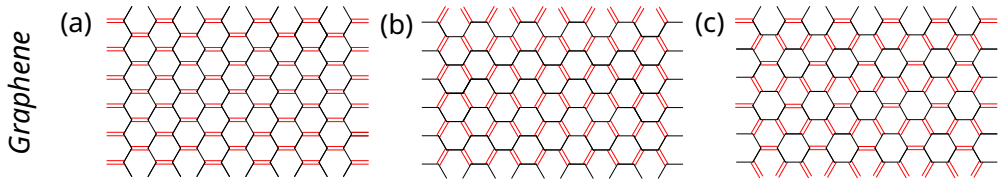

FIG. 4. Possible arrangements of sp^2 double bonds in an infinite graphene monolayer: (a) aligned along one of three equivalent directions, (b) aligned along two directions, and (c) aligned along three directions. (Double bonds: red; single bonds: black.)

atoms in the primitive cell equals 12. *Cmm*2-GmO concludes the first group of modeled GmO phases containing C atoms with four bonds.

The second group of the GmO family includes phases that have C atoms with three bonds (sp^2) [Fig. 2(e) to 2(h)]. They exclude the presence of 1,3-dioxetanes because of the restriction on the number of bonds connected to every C atom. As was seen in the previous group, 1,3-dioxetanes tend to be perpendicular to the center plane of the monolayer, with the O atoms above and below. In the sp^2 case, this would leave all C atoms with a single bond for in-plane connections, which would not build a stable structure. In this work, we explored only structures with sp^2 C atoms that were made of double-bonded C=C [Fig. 1(d)] with linking O atoms arranged in C–O–C-ether-like parts ($C222$-, *Pman*-, and $C2/m$-GmO) or carbonyls (*Cmma*-GmO).

$C222$-, *Pman*-, and $C2/m$-GmO were selected from the structures built assuming that alternative forms of GmO could contain C–O–C ethers instead of 1,3-dioxetanes. $C222$-, *Pman*-, and $C2/m$-GmO have negative formation energies of -0.38, -0.63, and -0.51 eV, respectively, and are reported here. A closer look at these models suggests that it would be misleading to say that these structures were built out of C–O–C ethers because this would imply two times as many C than O atoms. Instead, primitive cells of these models [Figs. 3(e) to 3(g)] are built from double-bonded C=C units with two linking O atoms that connect each C=C unit to other C=C units, i.e., these structures are built from sp^2 bonds formed on [(C=C) + 2O] units. The key differences between these models arise from the positioning of the linking O atoms above or below the center plane. Lattice parameters are influenced by tilts of the sp^2 bonds (or [(C=C) + 2O] units) that tend to stay planar. This tendency to stay in one plane is responsible for the complicated structure of $C2/m$-GmO that has three layers of C atoms with C=C double bonds aligned in the same direction.

$C222$-GmO [Fig. 2(e)] is the simplest phase made of [(C=C) + 2O] pieces. With a lattice constant of 3.50 Å and an opening angle of 106°, its rhombic primitive cell contains only two C and two O atoms connected in the [(C=C) + 2O] unit [Fig. 3(e)]. While the center plane consists only of C atoms, the flat sp^2 bonds are tilted by 26° with respect to the center plane, resulting in half of O atoms to be located above the cente plane, and the other half below.

At first glance, the primitive cell of *Pman*-GmO [Figs. 3(f) and 2(f)] resembles a centered rectangular version of $C222$-GmO containing 2 [(C=C) + 2O] units, or two sets of sp^2 bonds. However, in *Pman*-GmO, these flat units are tilted in opposite directions with respect to the center plane: the first unit is tilted by +39° and the second is tilted by −39°. The arrangement of the units placed this way proved to be unaffected by the size of periodic (super)cells used in the computations. Thus, *Pman*-GmO is a different GmO phase with different bond lengths ($a = 5.60$ Å, $b = 3.63$ Å).

$C2/m$-GmO [Figs. 3(g) and 2(g)] is the most complicated phase of the three structures made of [(C=C) + 2O] units. Unlike the previous two, C atoms in $C2/m$-GmO are located not only in the center plane, but also share the planes above and below with O atoms. It is the only GmO phase that has

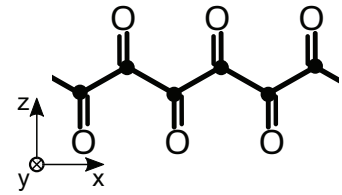

FIG. 5. Skeletal structure of the poly-CO chain. Side view: All atoms are located in the xz plane. Positions of C atoms are marked with solid circles.

three planes of C atoms. At the same time, O atoms can be found only in the upper and lower planes, at approximately the same heights as upper and lower C atoms: the C atoms at ±1.12 Å and the O atoms at ±1.17 Å relative to the center plane. In the primitive cell, two [(C=C) + 2O] units that are responsible for the formation of the upper and lower planes are almost flat and parallel to the center plane, while the other two [(C=C) + 2O] units that contain C atoms from the center plane are flat and rotated by ±80° with respect to the center plane. The latter two units connect the upper and lower planes. In total, the rhombic primitive cell of $C2/m$-GmO contains eight C and eight O atoms. With a lattice constant of 6.22 Å and opening angle of 127°, this primitive cell has the biggest area—and number of atoms—among all the primitive cells of considered GmO phases.

Cmma-GmO [Fig. 2(h)] is a 2D structure with the most negative calculated formation energy, −0.69 eV/atom in our modeling. It also has all C atoms with three bonds (one C=O and two C–C), but it is the only model made of vertical (along the z axis) C=O carbonyls oriented up and down and arranged in rows of repeated poly-CO chains (see Fig. 5) [20]. The primitive cell of *Cmma*-GmO [Fig. 3(h)] contains two C=O carbonyls: one with C and O atoms above the center plane (O on the top), and the other with C and O atoms below the center plane (O on the bottom). While the C atoms are located at ±0.43 Å above and below the center plane, the O atoms are at ±1.65 Å, the largest out-of-plane position of O atoms in the reported phases.

Composed of poly-CO chains, *Cmma*-GmO is a 2D equivalent to the $P2_1/m$ and *Pnma* chainlike 3D solid CO phases reported by Sun *et al.* [27]. Sun *et al.* also concluded that 3D solid CO phases made of poly-CO chains would be metallic and more stable than molecular phases of CO at zero temperature and pressure. Our computations revealed that the formation energy of isolated poly-CO chains is 0.01 eV more negative (−0.70 eV/atom) than *Cmma*-GmO. During computation of the elastic properties, it became clear that poly-CO chains in *Cmma*-GmO have very weak van der Waals interaction between the chains. For this reason, *Cmma*-GmO is the only structure where the introduction of vdW corrections changed the parameters of the primitive cell: vdW corrections did not influence any bond length or angle in the poly-CO chains, but reduced the separation between the chains from 3.09 Å to 2.93 Å, changing b from 6.19 to 5.85 Å.

Structural and crystallographic properties for the GmO phases are summarized in Table I. The first group of structures

TABLE I. Structural properties for GmO phases, graphene, poly-CO, and isolated 1,3-dioxetane unit. Cell types: <> rhombic (primitive), ▭ rectangular (primitive), ⋈ centered rectangular (nonprimitive), ⊢ 1D cell, • point group. N denotes the number of atoms in the primitive cell. ΔE is formation energy per atom relative to graphene and gas phase O_2 molecules. γ is the angle between lattice vectors $\boldsymbol{a}$ and $\boldsymbol{b}$. x and y are fractional coordinates of atoms in terms of lattice vectors $\boldsymbol{a}$ and $\boldsymbol{b}$. h is the height of atoms in Å. *Site* is the Wyckoff label of the atom. Space group symmetries and site labels can be found in [40].

Structure	Space group	ΔE (eV/atom)	Cell	N	a (Å) b (Å)	γ (°)	Atoms	x	y	h (Å)	Site
α-GmO	*Cmmm*	−0.58	⋈	8	5.67	90	C	0.174	0	0	4*g*
					2.64		O	0	0	1.04	4*k*
α-GmO[120]	*Cmmm*	−0.32	⋈	8	5.09	90	C	0.179	0	0	4*g*
					2.94		O	0	0	1.08	4*k*
β-GmO	*P*6/*mmm*	−0.51	<>	12	5.17	120	C	0.025	0.359	0	6*j*
							O	0.333	0.167	1.04	6*i*
Pmam-GmO	*Pmam*	−0.52	▭	8	4.98	90	C	0.084	0.712	0	4*i*
					3.08		O	0	0	1.04	4*g*
*Cmm*2-GmO	*Cmm*2	−0.61	⋈	24	9.38	90	C_1	0	0.309	0	4*e*
					5.23		C_2	0.135	0.142	0	8*f*
							O_1	0	0.500	1.04	2*b*
							O_2	0	0.500	−1.04	2*b*
							O_3	0.162	0	−1.18	4*d*
							O_4	0.250	0.250	0.67	4*c*
*C*222-GmO	*C*222	−0.38	⋈	8	5.61	90	C	0.120	0.500	0	4*e*
					4.20		O	0.250	0.250	−0.51	4*k*
Pman-GmO	*Pman*	−0.63	▭	8	5.60	90	C	0.119	0	0	4*e*
					3.63		O	0.250	0.250	−0.74	4*g*
*C*2/*m*-GmO	*C*2/*m*	−0.51	⋈	32	5.58	90	C_1	0	0.190	0	4*g*
					11.11		C_2	0	0.311	0	4*g*
							C_3	0.249	0.060	1.12	8*j*
							O_1	0.034	0.124	1.17	8*j*
							O_2	0.036	0.376	−1.17	8*j*
Cmma-GmO	*Cmma*	−0.69	⋈	8	2.57	90	C	0	0.250	0.43	4*g*
					6.19		O	0	0.250	1.65	4*g*
Graphene	*P*6/*mmm*		<>	2	2.46	120	C	1/3	2/3	0	2*c*
poly-CO	*p*2*mg*	−0.70	⊢	4	2.57		C	0.250		0.43	2*c*
							O	0.250		1.65	2*c*
1,3-dioxetane	*m*2*m*	+0.59	•	4	1.96		C	0.500		0	2*a*
							O	0		1.00	2*b*

are GmO phases that have C atoms with four bonds, and the next group are phases that have C atoms with three bonds. At the bottom of the table, the corresponding parameters for graphene, isolated poly-CO chains, and isolated 1,3-dioxetane unit are given as a reference. The formation energies are given with respect to ideal graphene and O_2 gas molecules. Table II compares bond lengths, angles, and atomic heights above the center plane (center axis) of the structures.

In Tables I and II, the poly-CO chain (Fig. 5) is presented as an infinite 2D stripe in the xz-plane with the chain being periodic only along the x (a) direction. In this configuration, the poly-CO chain belongs to the 2D space group *p*2*mg*. The C and O atoms are at ±0.43 and ±1.65 Å, respectively, relative to the chain's center axis. C=O and C–C bonds in poly-CO are 1.21 and 1.55 Å, respectively, and angle ∠CCC is 112°. Chains in *Cmma*-GmO have the same corresponding bond lengths and angles regardless of whether vdW corrections are used. Our results for the poly-CO chain are close to other DFT computations performed with different pseudopotentials [23].

1,3-dioxetane [Fig. 1(a)] implies an isolated nonrepeated unit containing two C and two O atoms arranged in configuration with *m*2*m* point-group symmetry. The C atoms are positioned around the origin on the x (a) axis at ±0.98 Å, while the O atoms are placed around the origin on the z axis at ±1.00 Å. An angle ∠COC of 88° is approximately the same as the corresponding 1,3-dioxetane angles in relaxed α-, β-, *Pmam*-, and *Cmm*2-GmO. The bond length of each of the four C–O bonds is 1.40 Å, which is ∼0.04 Å smaller than for the C–O bonds in 1,3-dioxetanes in the relaxed α-, β-, *Pmam*-, and *Cmm*2-GmO monolayers, but about the same as in the experimental α-GmO[120] structure. Thus, a change of the C–O bond length (and resulting O height) is the biggest difference between the isolated and GmO-embedded 1,3-dioxetane units. The positive formation energy of +0.59 eV/atom suggests that 1,3-dioxetane cannot exist as a standalone unit, which can be explained by the fact that each C atom in 1,3-dioxetane has only two bonds and needs to form two more bonds out of the plane of 1,3-dioxetane to reach sp^3 hybridization.

TABLE II. Bond lengths and angles of the GmO phases, graphene, poly-CO, and isolated unit of 1,3-dioxetane. Bond lengths, C heights h_C, and O heights h_O are in Å. Angles are in degrees. In $C222$-, *Pman*-, and $C2/m$-GmO, C–C implies C=C double bond. In poly-CO, C–O implies C=O double bond.

	Bond lengths			Bond angles			
Structure	C–O	C–C[a]	C,C[b]	∠COC	∠CCC	h_C	h_O
α-GmO	1.44	1.58	1.97	87	114	0	±1.04
α-GmO$^{120^\circ}$	1.41	1.64	1.83	80	128	0	±1.08
β-GmO	1.43	1.60	1.98	87	120	0	±1.04
Pmam-GmO	1.43	1.55	1.96	87	123	0	±1.04
		1.66					
*Cmm*2-GmO	1.44	1.54	2.43	123	111	0	1.03
	1.42	1.49	2.00	88			0.67
	1.39			63			−1.18
$C222$-GmO	1.37	1.35	2.55	138		0	±0.49
Pman-GmO	1.38	1.34	2.33	115		0	±0.74
$C2/m$-GmO	1.39	1.34	2.29	111		±1.12	±1.17
Cmma-GmO	1.21	1.55			112	±0.43	±1.65
Graphene		1.42			120	0	
poly-CO	1.21	1.55			112	±0.43	±1.65
1,3-dioxetane	1.40		1.96	88		0	±1.01

[a]Bridge between two physically connected C atoms.
[b]Distance between two nonconnected C atoms measured in the 1,3-dioxetane or C–O–C ether configurations.

B. Elastic properties

Investigation of the elastic properties of the GmO phases is important based on the fact that the only two phases confirmed in experiments were found in composites with graphene. One of the two phases, α-GmO, adjusted its lattice to the surrounding graphene lattice, while the other, β-GmO, was discovered in its relaxed state as predicted by DFT, which could be explained by β-GmO and graphene belonging to the same space group $P6/mmm$. However, none of the other modeled phases has the same symmetry as graphene. Hence, those phases, if discovered, would most likely also adjust their lattice depending on the synthesis process if they are soft compared to the graphene found in the composite. Thus, information regarding the elastic properties of the various phases is relevant.

Elastic moduli of the GmO models are summarized in Table III and compared to the corresponding experimental and theoretical moduli of graphene [50,53,56,57], as well as some previously calculated moduli of α-GmO [9]. The results in the present work are in good agreement with previous results for graphene and α-GmO. In general, the values of all of the moduli but C_{12} are at least 25% higher for graphene than for GmO phases. Unlike graphene, GmO phases are easy to distort by applied strains.

The 2D Young's moduli Y_1 and Y_2 characterize how easily the monolayers can be distorted along the $\boldsymbol{a}$ and $\boldsymbol{b}$ lattice vectors, respectively. In α-GmO, it is harder to change bond lengths and angles in 1,3-dioxetanes than to deform the C–C bonds, as seen from the higher value of the Young's modulus along the armchair direction, defined by armchairs with 1,3-dioxetanes (modulus Y_1), than along the zigzag direction that is made of ...–C–C–C–... zigzags (modulus Y_2). As in graphene, the two Young's moduli of β-GmO are equal due to the higher symmetry of the monolayer.

Computations of C_{11} and C_{22} constants for *Cmma*-GmO revealed the almost negligible connection between the poly-CO chains. When the monolayer was pulled in the direction perpendicular to the chains, the total energy decreased towards the isolated poly-CO chains limit. Hence, the corresponding modulus C_{22} of *Cmma*-GmO is identified as <0 in Table III: the energy curve did not have a local minimum on a range of applied strain, but monotonically decreased on the entire range. (An elastic modulus <0 means that the energy function is not quadratic and is not applicable to the theory of elasticity used in this work and thus a definite value is not given.) Inclusion of the vdW corrections did not change the energy behavior and left C_{22} negative and only slightly modified C_{11} (the modulus in the direction along the chains) from 140 to 146 N/m, a change that can be considered within the ±10 N/m error of our computations. Because of the negative C_{22}, it is impossible to find a value of C_{12} (and hence Y_i) in *Cmma*-GmO since the latter is derived from C_{11} and C_{22} via Eq. (10).

The elastic modulus C_{12} defines the dependence of the distortion along one direction on the other, e.g., a bigger C_{12} means a is more responsive to any change of b, and vice versa, cf. Eq. (10). Based on the values of C_{12}, $C222$-GmO has the strongest coupling between a and b, 30% higher than of graphene, and is the only GmO phase with C_{12} higher than of graphene. The second highest C_{12} of 40 N/m belongs to *Pman*-GmO, which is two times smaller than that of $C222$-GmO. Although elastic constants C_{11} and C_{22} are numerically close to the corresponding 2D Young's moduli Y_1 and Y_2 for most phases, the larger values of C_{12} in $C222$- and *Pman*-GmO make the Young's moduli significantly smaller than the corresponding diagonal elastic moduli [cf. Eq. (12)].

As can be seen from the transformation in Eq. (11), 2D shear is described by C_{66} which introduces perpendicular distortions to originally orthogonal lattice vectors $\boldsymbol{a}$ and $\boldsymbol{b}$.

TABLE III. Computed elastic constants of the GmO phases and graphene. Cell types: ▭ rectangular (primitive), ⋈ centered rectangular (nonprimitive). N denotes a number of atoms in the cells that were used. Lattice parameters of (centered-) rectangular cells, a and b, are in Å; elastic constants C_{ij}, Y_i, and B_{2D} are in N/m. For directions of x, y, a, and b axes, refer to Fig. 2.

Structure	Method	Lattice				C_{11}	Y_1	C_{22}	Y_2	C_{12}	$C_{66} \equiv G_{2D}$	B_{2D}
		Cell	N	a	b							
Graphene		⋈	4	4.26	2.46	350	340	350	340	60	140	200
α-GmO	DFT	⋈	8	5.67	2.64	280	280	210	210	10	60	120
β-GmO	this work	⋈	24	5.17	8.97	220	210	220	210	30	90	120
Pmam-GmO		▭	8	4.98	3.08	200	200	230	220	20	80	120
*Cmm*2-GmO		⋈	24	9.38	5.23	180	170	210	210	30	70	110
*C*222-GmO		⋈	8	5.63	4.14	180	130	120	80	80	80	110
Pman-GmO	DFT	▭	8	5.60	3.63	200	170	60	50	40	30	90
*C*2/*m*-GmO	this work	⋈	32	5.58	11.11	70	60	230	220	20	20	80
Cmma-GmO		⋈	8	2.57	6.19	140		<0			<10	50
Graphene	Experiment [56]						340 ± 50		340 ± 50			
Graphene	DFT [50]	⋈	4	4.24	2.45	358.1	347.9	358.1	347.9	60.4	148.9	209.3
Graphene	DFT [57]	⋈	4	4.35	2.51	360.7	352.5	360.7	352.5	54.3	152.5	207.5
Graphene	Theory[a] [58]	⋈	4	4.26	2.46	405.5	384.4	405.5	384.4	92.4	156.6	249.0
Graphene	DFT & MD[b] [53]	⋈	4	4.26	2.46		320		320			200
α-GmO	DFT [9]	⋈	8	5.67	2.65		295		191			

[a]Elastic constants derived from experimental phonon dispersions.
[a]Molecular dynamics.

β-GmO demonstrates the highest resistance to shear among the GmO phases that can be seen from the 2D shear modulus C_{66} of 90 N/m. However, this C_{66} is 35% smaller than the 140 N/m value in graphene. While β-GmO has the highest shear modulus among the α-, β-, and *Pmam*-GmO phases built exclusively of 1,3-dioxetanes, the 10% lower shear modulus of 80 N/m in *Pmam*-GmO and 30% lower shear modulus of 60 N/m in α-GmO highlight the decrease of resistance to shear with decreasing number of directions 1,3-dioxetane units are aligned in. A small 2D shear modulus can also result from a big difference between C_{11} and C_{22}. α-, *Pman*-, *C*2/*m*, and *Cmma*-GmO have the largest absolute differences ($|C_{11} - C_{22}|$) between the two moduli: 70, 140, 160, and >140 N/m, respectively, resulting in shear moduli of 60, 30, 20, and <10, respectively.

α-, β-, and *Pmam*-GmO have the same 2D bulk (B_{2D}) modulus of 120 N/m, i.e., they show similar resistance to uniform expansions and compressions. These are the highest bulk moduli among all GmO phases. The similarity can be explained by the fact that only these three phases are made exclusively of 1,3-dioxetane building units created on the C=C bonds of the original graphene structure. At the same time, the 2D bulk modulus of graphene is 67% larger.

For *Cmma*-GmO, the bulk modulus could not be derived from C_{11}, C_{22}, and C_{12} via Eq. (11) since C_{22} was negative and C_{12} not defined. Instead, explicit computations dilating the crystal, Eq. (13), were made. As in the case of the modulus C_{11}, B_{2D} stayed at 50 N/m regardless of whether vdW corrections were included. The bulk modulus of *Cmma*-GmO is the smallest among all the GmO phases, which is a direct consequence of almost absent interaction between poly-CO chains.

Summarizing the results from Table III, none of the GmO phases are as strong as graphene in terms of the elastic constants. Hence, if any of these phases is produced in a composite with graphene (or other strong monolayers), the GmO phase will most likely adjust its lattice parameters in response to the external constraints imposed by the other component. Table III also provides information regarding the directional difference in the elastic response of the structures that might indicate how they will adapt to a specific environment.

C. Electronic properties

Electronic band structures and densities of states for eight GmO phases are shown in Fig. 6. Table IV summarizes the calculated band gaps of the GmO phases and a single infinite poly-CO chain.

All the relaxed GmO phases, other than *Cmma*-GmO, are insulators or semiconductors, with the largest calculated gaps ~4 eV. (These gaps are expected to be lower bounds on the experimental ones due to the standard DFT underestimate of gaps [59].)

As was discussed above, all GmO phases are soft and can change their lattice parameters easily. When relaxed α-GmO structure is constrained to the lattice parameters of the

TABLE IV. Calculated band gaps in eV for the GmO phases.

Structure	Band gap	Direct/Indirect
α-GmO	0.58	Indirect (M-Γ)
α-GmO$^{120°}$	0	Direct (M)
β-GmO	1.18	Direct (Γ)
Pmam-GmO	2.08	Indirect (X'-Γ)
*Cmm*2-GmO	4.02	Indirect (Γ-K_S)
*C*222-GmO	1.54	Indirect (Γ -Δ)
Pman-GmO	4.12	Indirect (X-Δ)
*C*2/*m*-GmO	0.67	Direct (M_S)
Cmma-GmO	0	
poly-CO	0	

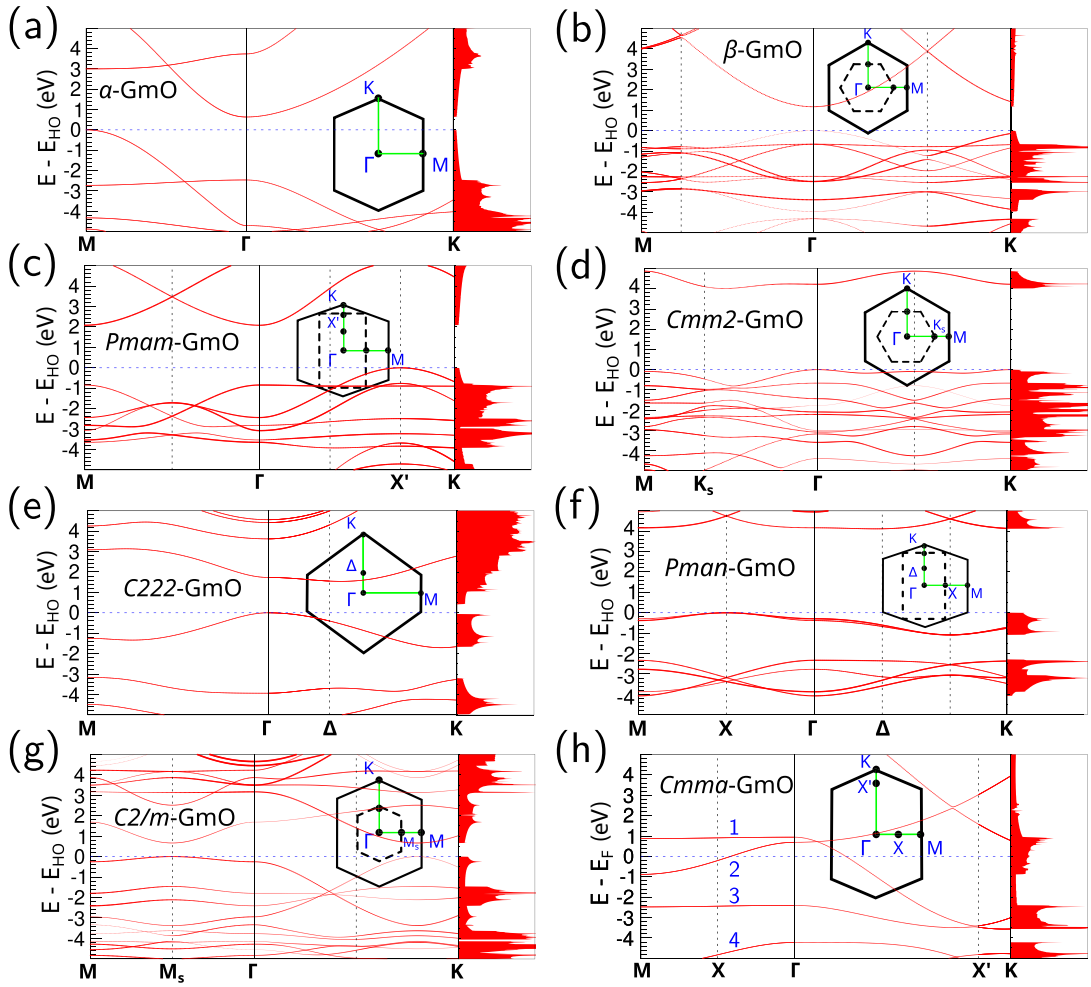

FIG. 6. Electronic band structures and densities of states of the GmO phases: (a) α-, (b) β-, (c) *Pmam*-, (d) *Cmm*2-, (e) *C*222-, (f) *Pman*-, (g) *C*2/*m*-, and (h) *Cmma*-GmO. Energies are given relative to the top of the valence band or Fermi level for metallic systems.

experimental α-GmO[120], its band gap closes at the M point, making the monolayer conducting. This is confirmed by the DFT map of the α-GmO band-gap dependence on lattice parameters in [8] and our present computations. Besides possible band-gap tuning by the surrounding graphene lattice in composites, later DFT studies of the interaction of α-GmO with Li showed that attached Li atoms can raise the Fermi level [13]. Similar considerations suggest that other GmO phases might change their conducting properties depending on the environment they exist in.

In metallic *Cmma*-GmO, Γ-K in reciprocal space corresponds to dispersion along the poly-CO chains, M-Γ to interactions between the chains. In the limit of infinite separation between the chains (isolated poly-CO chains), M-Γ compresses to a single Γ point, and the bands along Γ-K stay almost unaffected. The behavior of the bands in Fig. 6(h) are the same with or without vdW correction. In Fig. 6(h), bands 1 and 3 are O states with charge densities located along the poly-CO chains. These bands along Γ-M are flat and their energies are equal to corresponding energies of an infinite isolated poly-CO chain at the Γ point, i.e., bands 1 and 3 are unaffected by proximity to the neighboring poly-CO chains in *Cmma*-GmO. In contrast, the dispersive bands 2 and 4 correspond to O states with charge densities extending in the space between the poly-CO chains. Their energy values at the X point are essentially equal to the corresponding energies of the infinite isolated poly-CO chain at the Γ point, demonstrating bonding/antibonding effects between the chains.

IV. DISCUSSION

All reported GmO phases provided in Table I have negative heats of formations, ranging from -0.32 to -0.69 eV/atom. This reasonably small variation suggests that these phases could coexist in the same composite, while formation of a single-phase GmO monolayer might be experimentally challenging.

The C–O bond lengths in GmO phases given in Table II are increased compared to the C≡O triple bond length of 1.13 Å in gas phase molecular CO [60]. For all the phases except *Cmma*, the C–O bond length is about 1.4 Å; in *Cmma*-GmO, C–O bond (technically, C=O) is 1.21 Å, highlighting its polymeric structure.

For the relaxed GmO phases, we did not find a strong correlation between their composition and the band gaps. Notably, the band gap can be easily modified when

distortions are applied. The tunable nonzero band gap for all GmO phases (except *Cmma*) appears to be a unique feature of the GmO family that could lead to applications in batteries and nanoelectronics.

Based on the number of bonds attached to C atoms, the eight GmO phases reported in this work are divided into two groups: sp^3 group with C atoms having four bonds (four models) and sp^2 group with C atoms having three bonds (four models). From the analysis of the elastic moduli (e.g., 2D bulk moduli), it is evident that the sp^3 phases of GmO are more rigid than the sp^2 forms. These sp^3 phases are strong mostly due to the presence of the out-of-plane 1,3-dioxetane rings that do not allow large changes to their bond lengths. In contrast, when other building units are used along with 1,3-dioxetanes or exclude 1,3-dioxetanes completely, the structures get softer. This can be the main reason why the only two phases of GmO discovered experimentally to date were built exclusively of 1,3-dioxetanes. It also suggests that another phase of GmO built of 1,3-dioxetanes—*Pmam*-GmO—is very likely to be found.

The sp^2 phases change their lattice parameters under applied strain easier. In the process, the sp^2 bonds attached to the same C atom tend to stay in a common plane. The generally weaker interaction between the components of the sp^2 phases, compared to sp^3, leads to important observations (below) about the downsides of the *C*222- and *Cmma*-GmO phases that may make them practically impossible to find in experiments.

A. *C*222- to *Pman*-GmO transition

The elastic constants of *C*222- and *Pman*-GmO suggest that these structures can be easily deformed. They are constructed from one and two [(C=C) + 2O] units per primitive cell, respectively. The rectangular primitive cell of *Pman*-GmO is a supercell of the rhombic primitive cell of *C*222-GmO, which, at first glance, differs only by the positioning of O atoms above or below the center plane. However, further analysis shows that the [(C=C) + 2O] units in *Pman*-GmO are tilted by 13° more with respect to the center plane than [(C=C) + 2O] units in *C*222-GmO.

During the calculations of the elastic moduli, it was noticed that the O atoms of *C*222-GmO can change their positioning with respect to the center plane when deformations extend beyond 1%: specifically, when deformation of *b*—along (–C–O–C–O–) zigzags—exceeds 4% ($|\delta| > 0.04$); biaxial compression goes above 1% ($\delta < -0.01$); shear exceeds 1% ($|\delta| > 0.01$); or deformation in transformation $\hat{D}_{12}$ exceeds 2% ($|\delta| > 0.02$). By changing their height, O atoms convert an already deformed *C*222-GmO monolayer to a deformed (with different lattice parameters) *Pman*-GmO monolayer. Notably, deformations of *a*—along the C=C bonds—did not lead to a phase transition, which can be explained by the higher Young's modulus in the ***a*** direction.

The reverse transformation from *Pman*- to *C*222-GmO was not observed. This behavior can be justified by the fact that the formation energy of the relaxed *Pman*-GmO monolayer is 0.25 eV/atom more negative than that of the relaxed *C*222-GmO structure and deformations of *Pman*-GmO are also more favorable energetically. Notably, the energy difference between *Pman*- and *C*222-GmO is about the same as between *ab initio* α-GmO and experimental α-GmO[120].

Taking into account that the *b* lattice constant of α-GmO needs to decrease by 10% to adjust to the experimental value of α-GmO[120], *C*222-GmO with its opening angle of 106° might be impossible to find in any composite with graphene. Furthermore, it might be impossible to produce a pure *C*222-GmO monolayer because even small distortions will convert the system to the *Pman*-GmO phase.

B. One-dimensional poly-CO, 2D *Cmma*-GmO, and 3D $P2_1/m$- and *Pnma*-CO

Composed of poly-CO chains, metallic 2D *Cmma*-GmO was the most promising phase of GmO to consider because it had the most negative formation energy among all phases of GmO considered here. Moreover, Sun *et al.* [27] concluded that the metallic $P2_1/m$ and *Pnma* chain-like 3D solid CO phases made of poly-CO chains would be more stable than molecular phases of CO at zero temperature and pressure. Due to similarities between these 3D CO solids and 2D *Cmma*-GmO, it was expected that DFT modeling would find that *Cmma*-GmO is a stable monolayer.

However, the elastic constant computations revealed almost negligible interactions between the poly-CO chains despite the dispersion seen in the band structure. As was mentioned previously, the introduction of the vdW corrections decreased the spacing between the poly-CO chains in *Cmma*-GmO by 5%, but other structural parameters and properties were not affected. However, the formation energy was slightly, but monotonically, decreasing as the separation between the chains increased. In the limit of an isolated poly-CO chain, the formation energy of an isolated poly-CO chain was 0.01 eV/atom more negative than of *Cmma*-GmO.

Poly-CO chains in the $P2_1/m$ chainlike 3D solid CO phase in the paper by Sun *et al.* [27] appear to be tilted, while planes of poly-CO chains in our *Cmma*-GmO computations were parallel to the *z* axis. In *Cmma*-GmO, we performed additional computations introducing random tilting of poly-CO chains around their center axis, but in all cases the poly-CO chains returned back to their vertical orientations regardless of the spacing between the chains.

To further address the interaction between the chains, the chains were aligned in an *AA*-stacking, rather than the previous *AB*-stacking. As for the *AB*-stacking, all *AA*-configurations relaxed to vertical orientation starting from randomly tilted chains, regardless of the distance between the chains. The formation energy of chains with *AA*-stacking was 0.01 eV/atom less negative than for *AB*-stacking, and none of the stackings resulted in a more negative formation energy than of an isolated poly-CO chain.

V. CONCLUSION

Novel 2D phases of graphene monoxide, including the previously experimentally reported and modeled α- and β-GmO phases, were constructed and investigated through *ab initio* DFT modeling. Their building units were identified and structural properties were summarized.

The DFT formation energies of the new structures were comparable to those of the experimentally known phases of GmO. One of the phases, *Pmam*-GmO in particular, was very similar to α- and β-GmO by construction, and thus it is likely to be found in future experiments.

Previous experimental work found α-GmO in composites with graphene with lattice parameters that differ from the DFT relaxed values. To address this question, full sets of elastic constants were computed for all the models based on the standard theory of elasticity in order to understand the mechanical properties.

From an analysis of the mechanical properties, it was concluded that *C*222-GmO might be impossible to find in experiment since it easily transforms into *Pman*-GmO when distortions exceed 1%. Another phase, *Cmma*-GmO—the only phase made of poly-CO chains—is very unlikely to arrange in a 2D monolayer due to almost negligible (and possibly weakly repulsive) interaction between the chains, despite this phase having the most negative formation energy among all GmO phases and the *ab initio* predictions of 3D CO solids made up of poly-CO chains in other papers. Elastic constants helped to rule these two structures out. The other six phases, including known α- and β-GmO, are promising candidates to exist in nature.

All the phases, excluding the chainlike *Cmma*-GmO, have nonzero and tunable band gaps in their relaxed state. It suggests that GmO phases potentially could find applications in nanoelectronics or as battery electrodes [61].

ACKNOWLEDGMENTS

This work was supported by the National Science Foundation (Grants No. EFMA-1741673 and No. IIP-1843306). We thank C. J. Hirschmugl and M. A. Schofield for discussions.

[1] E. C. Mattson, H. Pu, S. Cui, M. A. Schofield, S. Rhim, G. Lu, M. J. Nasse, R. S. Ruoff, M. Weinert, M. Gajdardziska-Josifovska, J. Chen, and C. J. Hirschmugl, Evidence of nanocrystalline semiconducting graphene monoxide during thermal reduction of graphene oxide in vacuum, ACS Nano **5**, 9710 (2011).

[2] Y. Zhu, S. Murali, W. Cai, X. Li, J. W. Suk, J. R. Potts, and R. S. Ruoff, Graphene and graphene oxide: Synthesis, properties, and applications, Adv. Mater. **22**, 3906 (2010).

[3] D. R. Dreyer, S. Park, C. W. Bielawski, and R. S. Ruoff, The chemistry of graphene oxide, Chem. Soc. Rev. **39**, 228 (2010).

[4] M. Acik, G. Lee, C. Mattevi, M. Chhowalla, K. Cho, and Y. J. Chabal, Unusual infrared-absorption mechanism in thermally reduced graphene oxide, Nat. Mater. **9**, 840 (2010).

[5] M. Acik, C. Mattevi, C. Gong, G. Lee, K. Cho, M. Chhowalla, and Y. J. Chabal, The role of intercalated water in multilayered graphene oxide, ACS Nano **4**, 5861 (2010).

[6] D. Radevych, M. Gajdardziska-Josifovska, C. J. Hirschmugl, M. A. Schofield, and M. Weinert, β-graphene monoxide: Two-dimensional crystal form of carbon monoxide, Phys. Rev. Mater. **6**, 074006 (2022).

[7] H. H. Pu, E. C. Mattson, S. H. Rhim, M. Gajdardziksa-Josifovska, C. J. Hirschmugl, M. Weinert, and J. H. Chen, First-principles studies on infrared properties of semiconducting graphene monoxide, J. Appl. Phys. **114**, 164313 (2013).

[8] H. H. Pu, S. H. Rhim, C. J. Hirschmugl, M. Gajdardziska-Josifovska, M. Weinert, and J. H. Chen, Strain-induced band-gap engineering of graphene monoxide and its effect on graphene, Phys. Rev. B **87**, 085417 (2013).

[9] H. H. Pu, S. H. Rhim, C. J. Hirschmugl, M. Gajdardziska-Josifovska, M. Weinert, and J. H. Chen, Anisotropic thermal conductivity of semiconducting graphene monoxide, Appl. Phys. Lett. **102**, 223101 (2013).

[10] H. J. Xiang, S.-H. Wei, and X. G. Gong, Structural motifs in oxidized graphene: A genetic algorithm study based on density functional theory, Phys. Rev. B **82**, 035416 (2010).

[11] J. Chen, M. Gajdardziska-Josifovska, C. Hirschmugl, E. Mattson, H. Pu, and M. Weinert, Synthesis and applications of graphene based nanomaterials, US Patent No. 9236633 (2016).

[12] J. Woo, K.-H. Yun, S. B. Cho, and Y.-C. Chung, Defect-induced semiconductor to metal transition in graphene monoxide, Phys. Chem. Chem. Phys. **16**, 13477 (2014).

[13] D. Radevych, M. Gajdardziska-Josifovska, C. J. Hirschmugl, and M. Weinert, Interaction of lithium with a monolayer of graphene monoxide, J. Phys. Chem. C **125**, 11820 (2021).

[14] J. Woo, K.-H. Yun, and Y.-C. Chung, Graphene monoxide bilayer as a high-performance on/off switching media for nanoelectronics, ACS Appl. Mater. Interfaces **8**, 10477 (2016).

[15] J. C. Raich and R. L. Mills, α-γ transition in solid nitrogen and carbon monoxide at high pressure, J. Chem. Phys. **55**, 1811 (1971).

[16] D. T. Cromer, D. Schiferl, R. LeSar, and R. L. Mills, Room-temperature structure of carbon monoxide at 2.7 and 3.6 GPa, Acta Crystallogr. C **39**, 1146 (1983).

[17] R. L. Mills, D. Schiferl, A. I. Katz, and B. W. Olinger, New phases and chemical reactions in solid CO under pressure, J. Phys. Colloques **45**, C8-187 (1984).

[18] A. I. Katz, D. Schiferl, and R. L. Mills, New phases and chemical reactions in solid carbon monoxide under pressure, J. Phys. Chem. **88**, 3176 (1984).

[19] R. L. Mills, B. Olinger, and D. T. Cromer, Structures and phase diagrams of N_2 and CO to 13 GPa by x-ray diffraction, J. Chem. Phys. **84**, 2837 (1986).

[20] G. Frapper, C.-X. Cu, M. Kertesz, J.-F. Halet, J.-Y. Saillard, G. Frapper, and C.-X. Cu, Can carbon monoxide polymerize? A theoretical investigation of polyketone, Chem. Commun. **20**, 2011 (1997).

[21] M. Lipp, W. J. Evans, V. Garcia-Baonza, and H. E. Lorenzana, Carbon monoxide: Spectroscopic characterization of the high–pressure polymerized phase, J. Low Temp. Phys. **111**, 247 (1998).

[22] S. Bernard, G. L. Chiarotti, S. Scandolo, and E. Tosatti, Decomposition and Polymerization of Solid Carbon Monoxide under Pressure, Phys. Rev. Lett. **81**, 2092 (1998).

[23] R. Podeszwa and R. J. Bartlett, Crystal orbital study of polycarbonyl, Int. J. Quantum Chem. **95**, 638 (2003).

[24] M. J. Lipp, W. J. Evans, B. J. Baer, and C.-S. Yoo, High-energy-density extended CO solid, Nat. Mater. **4**, 211 (2005).

[25] W. J. Evans, M. J. Lipp, C.-S. Yoo, H. Cynn, J. L. Herberg, R. S. Maxwell, and M. F. Nicol, Pressure-induced polymerization of carbon monoxide: Disproportionation and synthesis of an energetic lactonic polymer, Chem. Mater. **18**, 2520 (2006).

[26] M. Ceppatelli, R. Bini, and V. Schettino, High-pressure reactivity of model hydrocarbons driven by near-UV photodissociation of water, J. Phys. Chem. B **113**, 14640 (2009).

[27] J. Sun, D. D. Klug, C. J. Pickard, and R. J. Needs, Controlling the Bonding and Band Gaps of Solid Carbon Monoxide with Pressure, Phys. Rev. Lett. **106**, 145502 (2011).

[28] K. Xia, J. Sun, C. J. Pickard, D. D. Klug, and R. J. Needs, Ground state structure of high-energy-density polymeric carbon monoxide, Phys. Rev. B **95**, 144102 (2017).

[29] P. Giannozzi, S. Baroni, N. Bonini, M. Calandra, R. Car, C. Cavazzoni, D. Ceresoli, G. L. Chiarotti, M. Cococcioni, I. Dabo, A. D. Corso, S. de Gironcoli, S. Fabris, G. Fratesi, R. Gebauer, U. Gerstmann, C. Gougoussis, A. Kokalj, M. Lazzeri, L. Martin-Samos *et al.*, QUANTUM ESPRESSO: A modular and open-source software project for quantum simulations of materials, J. Phys.: Condens. Matter **21**, 395502 (2009).

[30] P. Giannozzi, O. Andreussi, T. Brumme, O. Bunau, M. B. Nardelli, M. Calandra, R. Car, C. Cavazzoni, D. Ceresoli, M. Cococcioni, N. Colonna, I. Carnimeo, A. D. Corso, S. de Gironcoli, P. Delugas, R. A. DiStasio, Jr., A. Ferretti, A. Floris, G. Fratesi, G. Fugallo *et al.*, Advanced capabilities for materials modelling with QUANTUM ESPRESSO, J. Phys.: Condens. Matter **29**, 465901 (2017).

[31] P. Giannozzi, O. Baseggio, P. Bonfà, D. Brunato, R. Car, I. Carnimeo, C. Cavazzoni, S. de Gironcoli, P. Delugas, F. Ferrari Ruffino, A. Ferretti, N. Marzari, I. Timrov, A. Urru, and S. Baroni, QUANTUM ESPRESSO toward the exascale, J. Chem. Phys. **152**, 154105 (2020).

[32] K. Momma and F. Izumi, *VESTA3* for three-dimensional visualization of crystal, volumetric and morphology data, J. Appl. Crystallogr. **44**, 1272 (2011).

[33] A. D. Corso, Pseudopotentials periodic table: From H to Pu, Comput. Mater. Sci. **95**, 337 (2014).

[34] S. Grimme, J. Antony, S. Ehrlich, and H. Krieg, A consistent and accurate ab initio parametrization of density functional dispersion correction (DFT-D) for the 94 elements H-Pu, J. Chem. Phys. **132**, 154104 (2010).

[35] S. Grimme, S. Ehrlich, and L. Goerigk, Effect of the damping function in dispersion corrected density functional theory, J. Comput. Chem. **32**, 1456 (2011).

[36] N. Mounet and N. Marzari, First-principles determination of the structural, vibrational and thermodynamic properties of diamond, graphite, and derivatives, Phys. Rev. B **71**, 205214 (2005).

[37] I. V. Lebedeva, A. V. Lebedev, A. M. Popov, and A. A. Knizhnik, Comparison of performance of van der Waals-corrected exchange-correlation functionals for interlayer interaction in graphene and hexagonal boron nitride, Comput. Mater. Sci. **128**, 45 (2017).

[38] H. T. Stokes, D. M. Hatch, and B. J. Campbell, ISOTROPY: Software Suite.

[39] H. T. Stokes and D. M. Hatch, FINDSYM: Program for identifying the space-group symmetry of a crystal, J. Appl. Crystallogr. **38**, 237 (2005).

[40] *International Tables for Crystallography*, edited by T. Hahn, (International Union of Crystallography, Chester, England, 2006).

[41] P. Villars, *Pearson's Handbook of Crystallographic Data for Intermetallic Phases* (American Society for Metals, Materials Park, OH, 1985).

[42] J. W. Davenport, R. E. Watson, and M. Weinert, Linear augmented-Slater-type-orbital method for electronic-structure calculations. V. Spin-orbit splitting in Cu_3 Au, Phys. Rev. B **37**, 9985 (1988).

[43] Y. Qi, S. H. Rhim, G. F. Sun, M. Weinert, and L. Li, Epitaxial Graphene on SiC(0001): More than Just Honeycombs, Phys. Rev. Lett. **105**, 085502 (2010).

[44] M. Chen and M. Weinert, Layer k-projection and unfolding electronic bands at interfaces, Phys. Rev. B **98**, 245421 (2018).

[45] M. X. Chen and M. Weinert, Revealing the substrate origin of the linear dispersion of silicene/Ag(111), Nano Lett. **14**, 5189 (2014).

[46] C. Kittel, *Introduction to Solid State Physics*, 8th ed., (Wiley, New York, 2004).

[47] L. Fast, J. M. Wills, B. Johansson, and O. Eriksson, Elastic constants of hexagonal transition metals: Theory, Phys. Rev. B **51**, 17431 (1995).

[48] P. Ravindran, L. Fast, P. A. Korzhavyi, B. Johansson, J. Wills, and O. Eriksson, Density functional theory for calculation of elastic properties of orthorhombic crystals: Application to $TiSi_2$, J. Appl. Phys. **84**, 4891 (1998).

[49] M. Faghihnasiri, A. Ahmadi, S. Alvankar Golpayegan, S. Garosi Sharifabadi, and A. Ramazani, A first-principles study of nonlinear elastic behavior and anisotropic electronic properties of two-dimensional HfS_2, Nanomaterials **10**, 446 (2020).

[50] X. Wei, B. Fragneaud, C. A. Marianetti, and J. W. Kysar, Nonlinear elastic behavior of graphene: Ab initio calculations to continuum description, Phys. Rev. B **80**, 205407 (2009).

[51] R. C. Andrew, R. E. Mapasha, A. M. Ukpong, and N. Chetty, Mechanical properties of graphene and boronitrene, Phys. Rev. B **85**, 125428 (2012).

[52] See Supplemental Material at http://link.aps.org/supplemental/10.1103/PhysRevB.107.054104 for 2D Young's moduli via elastic constants and structures in multiple views.

[53] G. Kalosakas, N. N. Lathiotakis, C. Galiotis, and K. Papagelis, In-plane force fields and elastic properties of graphene, J. Appl. Phys. **113**, 134307 (2013).

[54] G. Cao, Atomistic studies of mechanical properties of graphene, Polymers **6**, 2404 (2014).

[55] K. M. Knowles, The biaxial moduli of cubic materials subjected to an equi-biaxial elastic strain, J. Elast. **124**, 1 (2016).

[56] A. King, G. Johnson, D. Engelberg, W. Ludwig, and J. Marrow, Observations of intergranular stress corrosion cracking in a grain-mapped polycrystal, Science **321**, 382 (2008).

[57] M. Niederreiter, Determining elastic constants of graphene using density functional theory, Bachelor's thesis, University of Graz, Austria, 2018.

[58] K. H. Michel and B. Verberck, Theory of the elastic constants of graphite and graphene, Phys. Status Solidi B **245**, 2177 (2008).

[59] M. van Schilfgaarde, T. Kotani, and S. Faleev, Quasiparticle self-consistent *GW* theory, Phys. Rev. Lett. **96**, 226402 (2006).

[60] K. P. Huber and G. Herzberg, Constants of diatomic molecules, in *Molecular Spectra and Molecular Structure: IV. Constants of Diatomic Molecules* (Springer, Boston, 1979), pp. 8–689.

[61] C. J. Hirschmugl, M. Gajdardziska-Josifovska, M. Schofield, Y. Kutsovsky, X. Huang, and D. Radevych, Graphene monoxide compositions of matter and electrodes comprising them (2021), U.S. Patent Application No. 17/148010, WIPO Publication No. WO/2021/206779, COnovate Inc. and University of Wisconsin-Milwaukee Research Foundation.